The mouse nicotinamide mononucleotide adenylyltransferase chaperones diverse pathological amyloid client proteins

Chengan Huang[1,2,‡], Jinxia Lu[1,2,‡], Xiaojuan Ma[3,4,‡], Jiali Qiang[3,4], Chuchu Wang[3,4], Cong Liu[3], Yanshan Fang[3], Yaoyang Zhang[3], Lin Jiang[5], Dan Li[1,2,6,*], and Shengnan Zhang[3,*]

From the [1]Bio-X Institutes, Key Laboratory for the Genetics of Developmental and Neuropsychiatric Disorders, Ministry of Education, and [2]Bio-X-Renji Hospital Research Center, Renji Hospital, School of Medicine, Shanghai Jiao Tong University, Shanghai, China; [3]Interdisciplinary Research Center on Biology and Chemistry, Shanghai Institute of Organic Chemistry, Chinese Academy of Sciences, Shanghai, China; [4]University of the Chinese Academy of Sciences, Beijing, China; [5]Department of Neurology, Molecular Biology Institute, and Brain Research Institute, UCLA, Los Angeles, California, USA; [6]Zhangjiang Institute for Advanced Study, Shanghai Jiao Tong University, Shanghai, China

Edited by Paul Fraser

Molecular chaperones safeguard cellular protein homeostasis and obviate proteotoxicity. In the process of aging, as chaperone networks decline, aberrant protein amyloid aggregation accumulates in a mechanism that underpins neurodegeneration, leading to pathologies such as Alzheimer's disease and Parkinson's disease. Thus, it is important to identify and characterize chaperones for preventing such protein aggregation. In this work, we identified that the NAD⁺ synthase–nicotinamide mononucleotide adenylyltransferase (NMNAT) 3 from mouse (mN3) exhibits potent chaperone activity to antagonize aggregation of a wide spectrum of pathological amyloid client proteins including α-synuclein, Tau (K19), amyloid β, and islet amyloid polypeptide. By combining NMR spectroscopy, cross-linking mass spectrometry, and computational modeling, we further reveal that mN3 uses different region of its amphiphilic surface near the active site to directly bind different amyloid client proteins. Our work demonstrates a client recognition mechanism of NMNAT via which it chaperones different amyloid client proteins against pathological aggregation and implies a potential protective role for NMNAT in different amyloid-associated diseases.

Molecular chaperone is the major component of protein homeostasis network that preserves cellular proteins from aberrant misfolding and aggregation (1–4). Deficiency of proteostasis network underpins accumulation of pathological protein aggregates in a variety of neurodegenerative disorders, including Alzheimer's disease (AD) and Parkinson's disease (PD) (5, 6). Many different neurodegenerative diseases share a common characteristic of amyloid protein fibrillation that is hazardous to cells and contributes to the disease initiation and progression (7–9). Canonical chaperones including Hsp70, Hsp40, and Hsp27 were found to play a vital role in antagonizing aberrant aggregation of different pathological amyloid proteins, for example, α-synuclein (α-syn), Tau, amyloid β (Aβ), and islet amyloid polypeptide (IAPP) in normal aging and disease conditions (10–17). It is important to identify and characterize different chaperones in recognizing and preventing protein aggregation, which may help to understand how cells maintain proteostasis and combat pathological protein aggregation.

Recently, nicotinamide mononucleotide adenylyltransferase, an enzyme that synthesizes NAD from nicotinamide mononucleotide (NMN) and ATP (18), was identified to be protective in different cellular and animal models of neurodegenerative diseases (19–23). The behaviors of NMNAT presented in these studies recall those of molecular chaperones (2, 3, 24). Moreover, NMNAT can recognize the pathological phosphorylated Tau (pTau) and prevent its amyloid fibrillation (25). However, it remains unclear whether NMNAT serves as a chaperone specifically for pTau or it exhibits a chaperone activity to a broad spectrum of amyloid client proteins like the canonical chaperones.

In this study, we identified that mouse NMNAT 3 (mN3) exhibits a broad chaperone activity of preventing various pathological proteins from amyloid aggregation including α-syn, Tau (K19), Aβ₄₀, and IAPP. By combining multiple biophysical approaches and mutagenesis study, we show that mN3 uses different part of a conserved pocket to bind multiple amyloid client proteins as for preventing their abnormal aggregation. Both electrostatic and hydrophobic interactions contribute to the client recognition and binding of mN3. Our work provides a mechanistic view of how NMNAT recognizes different pathological amyloid client proteins and prevents their amyloid aggregation.

Results

mN3 chaperones various amyloid proteins against aggregation

To investigate whether NMNAT can directly chaperone amyloid proteins against aggregation, we tested the effects of NMNAT on a variety of disease-associated pathological

amyloid proteins including α-syn of PD (26), Tau (K19) and Aβ$_{40}$ of AD (27), and IAPP of type II diabetes (28), respectively. NMNAT exists in three isoforms including NMNAT 1 (N1), NMNAT 2 (N2), and NMNAT 3 (N3), which share high sequence similarities (Fig. S1). We successfully purified recombined mouse N1 (mN1) and N3 (mN3) (Fig. 2A), while mouse N2 (mN2) was not expressed in *Escherichia coli*. As mN3 exhibits better protein stability than mN1 as measured by their Tm values (Fig. S2B), we chose to use mN3 for the following *in vitro* biophysical and biochemical experiments. As shown in Figure 1, A and B, at substoichiometric molar ratios of mN3 to amyloid client protein (1:100, 1:50, and 1:5), mN3 remarkably inhibited the fibril formation of all four amyloid client proteins in a concentration-dependent manner revealed by both thioflavin T (ThT) fluorescence kinetics assay and negative-stain transmission electron microscopy. In addition, the inhibitory effect of mN3 on these four amyloid protein clients is comparable to that of a canonical chaperone Hsp27 (Fig. 1, A and B). Together, our results demonstrate that mN3 can prevent the aggregation of different pathological amyloid client proteins.

mN3 binds to the C-terminal region of α-syn

Next, we sought to study the structural basis underlying the interaction of mN3 and the client amyloid protein by focusing on α-syn, which is the key pathological amyloid protein in PD and other synucleinopathies (26, 29). We firstly used the bio-layer interferometry (BLI) assay to measure the binding affinity between α-syn and mN3. The result shows that mN3 binds to α-syn with an equilibrium dissociation constant (K_D) of 1.90 ± 0.03 μM (Fig. S3). We then conducted solution NMR spectroscopy to identify the residues of α-syn that are involved in mN3 binding. We used mN3 to titrate ^{15}N-labeled α-syn and observed that some of the crosspeaks in the overlaid HSQC spectra reveal a concentration-dependent signal reduction and chemical shift changes (Fig. S4). Notably, a prominent signal reduction ($I/I_0 < 0.25$) as well as chemical shift changes (mostly >0.02 ppm) occurred at residues 112 to 140 upon addition of 2 M folds of mN3 to ^{15}N-α-syn (Fig. 2, A and B), indicating that the C-terminal region of α-syn is predominantly involved in mN3 binding. Then, we truncated the C-terminal region of α-syn (residues 101–140, the resulting construct was termed as α-syn$_{1-100}$) to disrupt the mN3–α-syn interaction, while kept the amyloid-forming ability by retaining the intact nonamyloid-component domain of α-syn. As shown in Figure 2, C and D, α-syn$_{1-100}$ can still form amyloid fibrils, whereas mN3 displays no inhibitory activity in inhibiting the amyloid formation of α-syn$_{1-100}$. As a control, epigallocatechin gallate, a small-molecule inhibitor of α-syn which nonspecifically binds to multiple regions across α-syn (30), can inhibit both α-syn and α-syn$_{1-100}$ amyloid aggregation (Fig. S5). Together, these results demonstrate that mN3 interacts with the C-terminus of α-syn to prevent its amyloid aggregation.

Of note, within the C-terminal region of α-syn, segments ^{114}EDMPVD^{119} and ^{134}QDYE^{137} exhibited the most drastic interaction with mN3 with a signal loss of over 90% and

chemical shift perturbations (>0.02 ppm) (Fig. 2, A and B). Intriguingly, these two segments are rich in negatively charged residues, implying that electrostatic interaction may play an important role in mediating mN3–α-syn interaction.

Electrostatic and hydrophobic interactions govern the mN3-α-syn binding

To further identify the interacting surface of mN3 for α-syn binding, we used a chemical cross-linker of BS^3 to covalently link two lysine residues in spatial proximity (Cα-Cα distance <24 Å) as α-syn and mN3 transiently bind, then identified the cross-linked segments by mass spectrometry (MS). The MS experiment identified 22 pairs of cross-linked segments between α-syn and mN3 with a confidence score of $<10^{-8}$ (Fig. 3 and Table S1). Strikingly, these pairs of segments were cross-linked through six lysine residues including K55, K56, K95, K139, K148, and K206 (Figs. 4A and S6), which spread around the entrance of the active site of mN3 (Fig. S7). Since the C-terminal 30 residues of α-syn were identified to be the interface binding with mN3 (Fig. 2, A and B), the peptide-containing residues of ^{111}GILEDMPVDPDNEAYEMPSEEGY QDYEPEA^{140} (α-syn$_{111-140}$) were used to build the complex structure of mN3 with α-syn by Rosetta remodeling (31). One top model of the mN3–α-syn$_{111-140}$ complex ranked by Rosetta energies and constraints were shown in Figure 4B, in which α-syn$_{111-140}$ is well accommodated on the active site of mN3. We then used both NMR and BLI assays to detect whether the binding of α-syn to mN3 is influenced by natural substrates of mN3 including ATP and NMN, since these substrates binds to the active site of mN3 (32). The chemical shift differences (CSDs) and intensity drop of α-syn caused by mN3 titration were almost completely restored after addition of 10 M folds of ATP to the NMR sample of ^{15}N-α-syn with mN3 (Fig. S8A), indicating that ATP in the buffer significantly weakens the interaction between α-syn with mN3. In addition, the response values in BLI assays decreased in a concentration-dependent manner with the increasing concentrations of ATP (Fig. S8B), suggesting that ATP competes with α-syn to bind mN3. Similar results were observed in both the NMR and BLI experiments with the addition of another natural substrate NMN (Fig. S8, C and D). Of note, the recovery of the CSD and intensity drop of α-syn caused by addition of NMN is a little smaller than that caused by ATP, and the decreased response values in the BLI experiments by addition of NMN is also smaller than that caused by ATP, implying that substrate ATP reveals a stronger competition against α-syn binding to mN3 than that of NMN. Taken together, these results demonstrate that both the two natural substrates including ATP and NMN compete with α-syn to bind mN3, which further validates our results that α-syn binds in close proximity to the active site of mN3.

Electrostatic surface of this interface of mN3 features a positively charged patch (Fig. 4B), where the negatively charged C-terminal region of α-syn may bind *via* electrostatic interactions. Indeed, the CSD and intensity drop of α-syn caused by mN3 titration were restored in a certain degree after
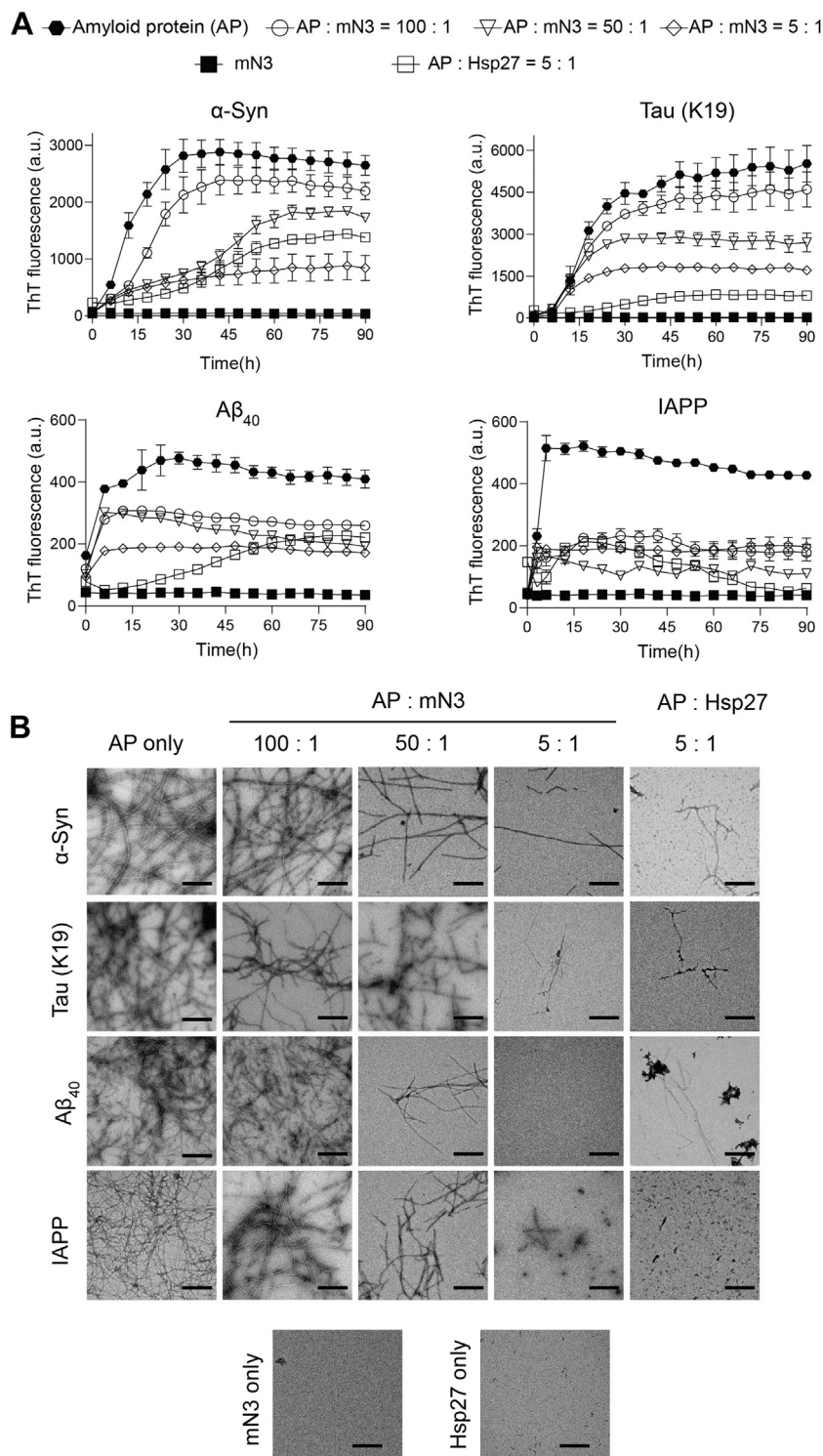
Figure 1. Inhibition of mN3 to the aggregation of various amyloid client proteins. *A*, effects of mN3 on the fibril formation of α-syn (100 µM), Tau K19 (100 µM), IAPP (50 µM), and Aβ$_{40}$ (30 µM) measured by ThT fluorescence assays, respectively. The canonical chaperone Hsp27 was used as a control. Amyloid client proteins were incubated with mN3 at different molar ratios as indicated. The error bars correspond to mean ± SEM, with n = 3. *B*, negative-stain TEM images of amyloid client proteins with the addition of mN3 after incubation at 37 °C for 90 h. The control images of mN3/Hsp27 only are shown at the *bottom*. The scale bars represent 500 nm. α-syn, α-synuclein; Aβ, amyloid β; IAPP, islet amyloid polypeptide; ThT, thioflavin T.

addition of 100 mM NaCl to the NMR sample of ^{15}N-α-syn with mN3 (molar ratio 1:2) (Fig. S9A), indicating that salt weakens the electrostatic interaction between α-syn with mN3. In addition, the response values in the BLI assay decreased in a concentration-dependent manner with the increasing concentrations of salt (Fig. S9B), demonstrating that salt decreases the binding between mN3 and α-syn. Taken together, these results further support that electrostatic interaction plays an
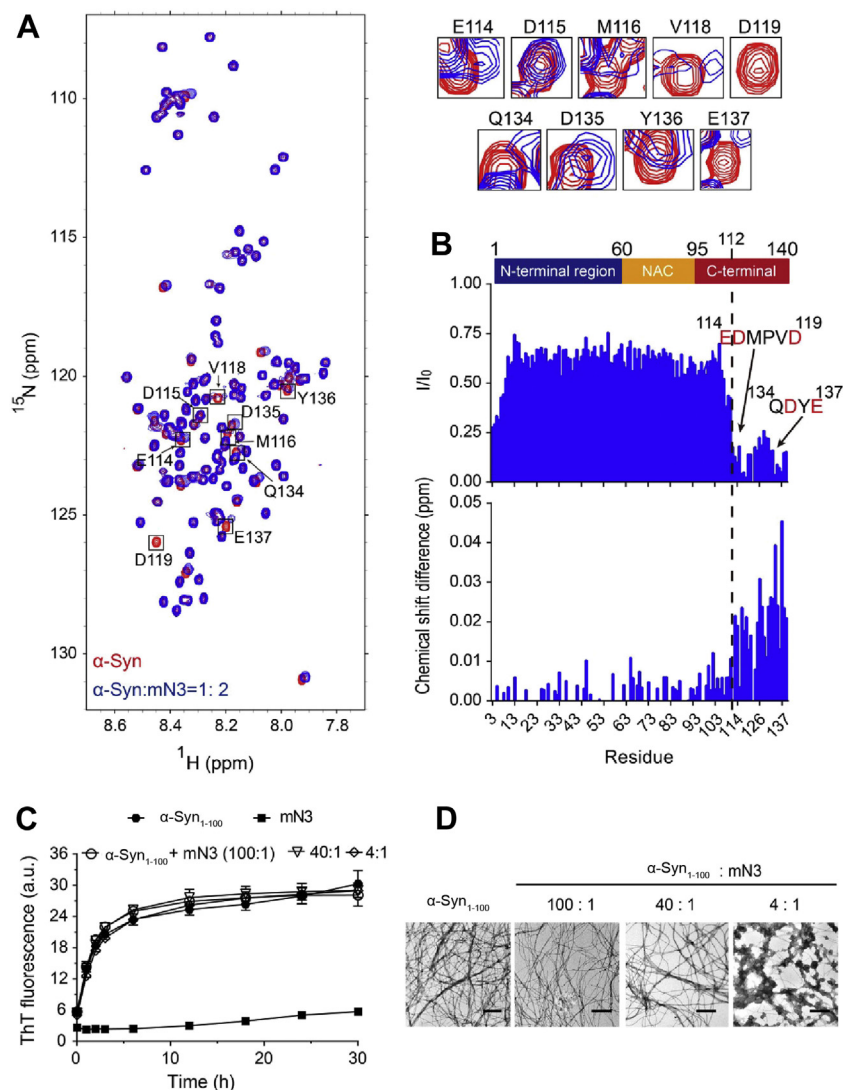
Figure 2. The C-terminal region of α-syn binds to mN3. *A*, overlay of the 2D ^{1}H-^{15}N HSQC spectra of α-syn alone (138 μM, *red*) and in the presence of mN3 (276 μM, *blue*). Residues that underwent significant resonance changes are zoomed in and labeled. *B*, residue-specific changes in the intensity (*top*) and chemical shift (*bottom*) of a-syn signals in (*A*). The combined chemical shift difference (CSD) was calculated using the empirical equation $\Delta CSD = [\Delta H_N^2 + (\Delta N/6.5)^2]^{1/2}$, where ΔH_N and ΔN represent the chemical shift differences of ^1H_N and ^{15}N, respectively. The domain organization of α-syn is indicated on the *top* of the graph. Segments that underwent the most significant resonance changes are labeled with the negatively charged residues highlighted in *red*. *C*, influence of mN3 on the amyloid aggregation of α-syn$_{1-100}$ (200 μM) measured by ThT assay. Error bars correspond to mean ± SEM, with n = 3. *D*, negative-stain TEM images of samples that after incubation of α-syn$_{1-100}$ with mN3 at 37 °C for 30 h. The scale bars represent 500 nm. α-syn, α-synuclein; ThT, thioflavin T; CSD, chemical shift difference.

important role in α-syn binding to mN3. And as we gradually increased the salt concentrations to weaken electrostatic interactions, the inhibitory effect of mN3 on α-syn aggregation was increasingly weakened (Fig. 4*C*). To further cross-validate, we mutated residues K55, K56, R205, and K206 to negatively charged glutamate (E) to disrupt the electrostatic interactions between mN3 and α-syn. We constructed double mutations of K55E and K56E (KK), R205E and K206E (RK), and a quadruple mutation of K55E, K56E, R205E, and K206E (KKRK) of mN3. ThT fluorescence assays showed that mutations of KK and KKRK significantly impaired the inhibition of mN3 to α-syn aggregation (Fig. 4*D*), further supporting the important role of electrostatic interactions in mN3-α-syn binding. Of note, disruption of the positively charged patch did not completely eliminate the chaperone activity of mN3, indicating that other

interaction also contributes to the binding of mN3 to α-syn. Considering that residues Y133-A140 of α-syn are tucked into the active site of mN3 in the modeled complex structure, especially that Y136 binds to the hydrophobic pocket of mN3 (Fig. 4*B*), hydrophobic interaction may also play a role in the interaction of mN3 with α-syn. Together, our results suggest that both electrostatic and hydrophobic interactions govern the interaction of mN3 with α-syn.

The interface of mN3 for binding Tau (k19), IAPP, and Aβ$_{40}$

To further characterize the interface of mN3 binding with other amyloid client proteins, we performed the cross-linking mass spectrometry (CX-MS) with linker BS^3 to cross-link the transient protein complex formed by mN3 and its amyloid client proteins including Tau (K19), IAPP, and Aβ$_{40}$,
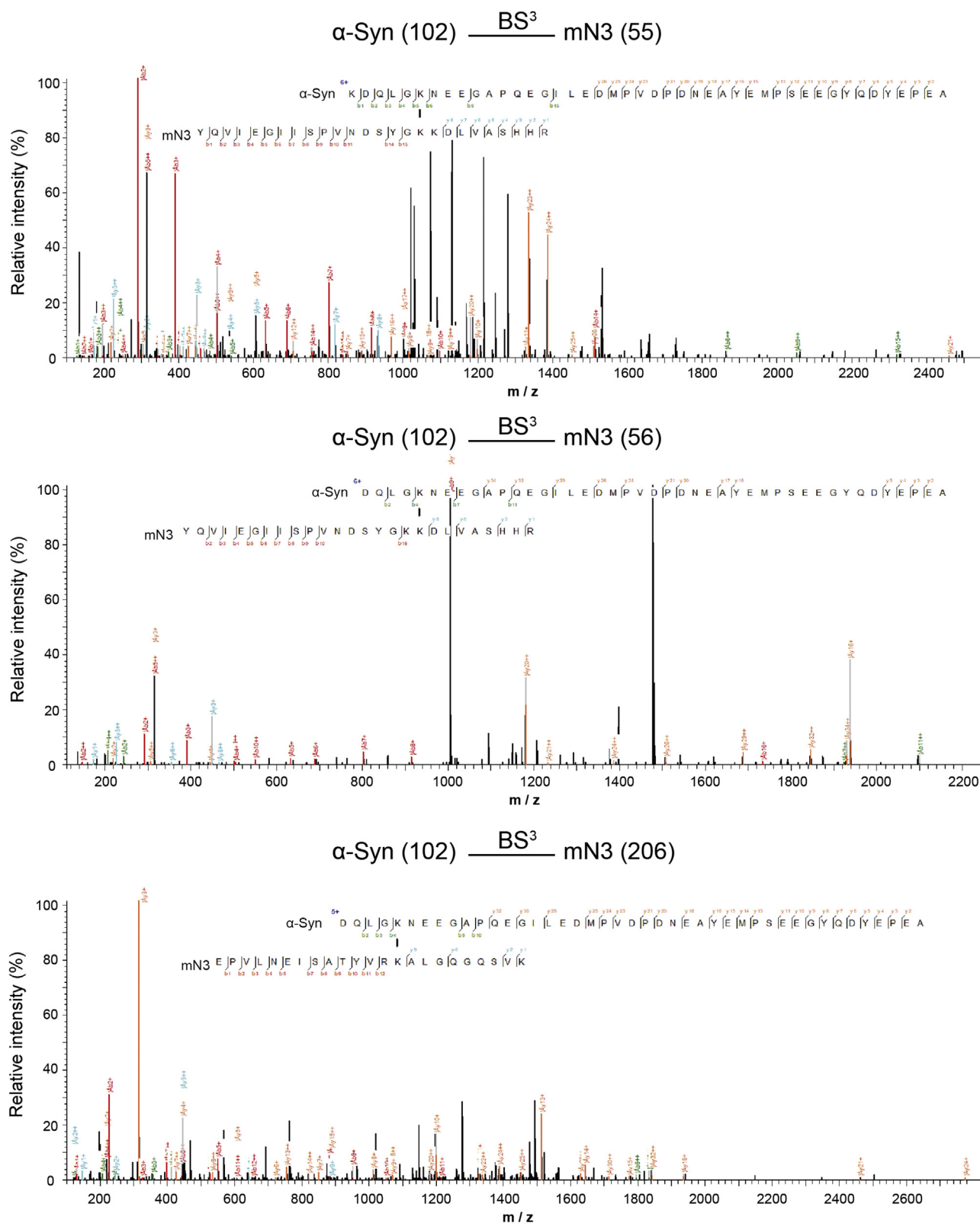
Figure 3. Representative MS spectra of the identified cross-linked peptides between mN3 and α-syn. Primary sequences of linked peptides are shown, with sites of cleavages labeled in different colors in both the sequences and spectra. 5+ or 6+ indicates the charge of the cross-linked peptides. α-syn, α-synuclein; MS, mass spectrometry.
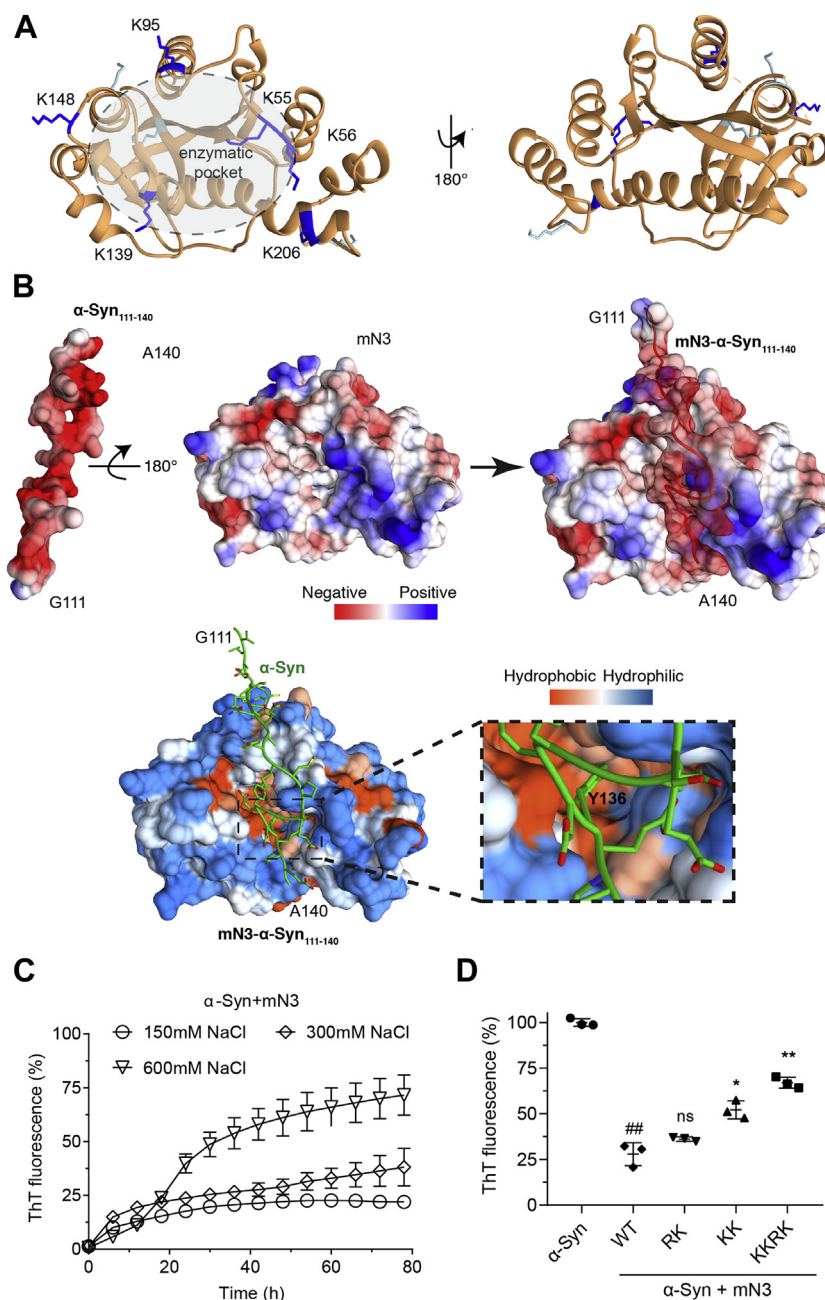
Figure 4. Structure basis of mN3 binding to α-syn. *A*, lysine resides that cross-linked with α-syn are shown as *sticks* in *blue* in the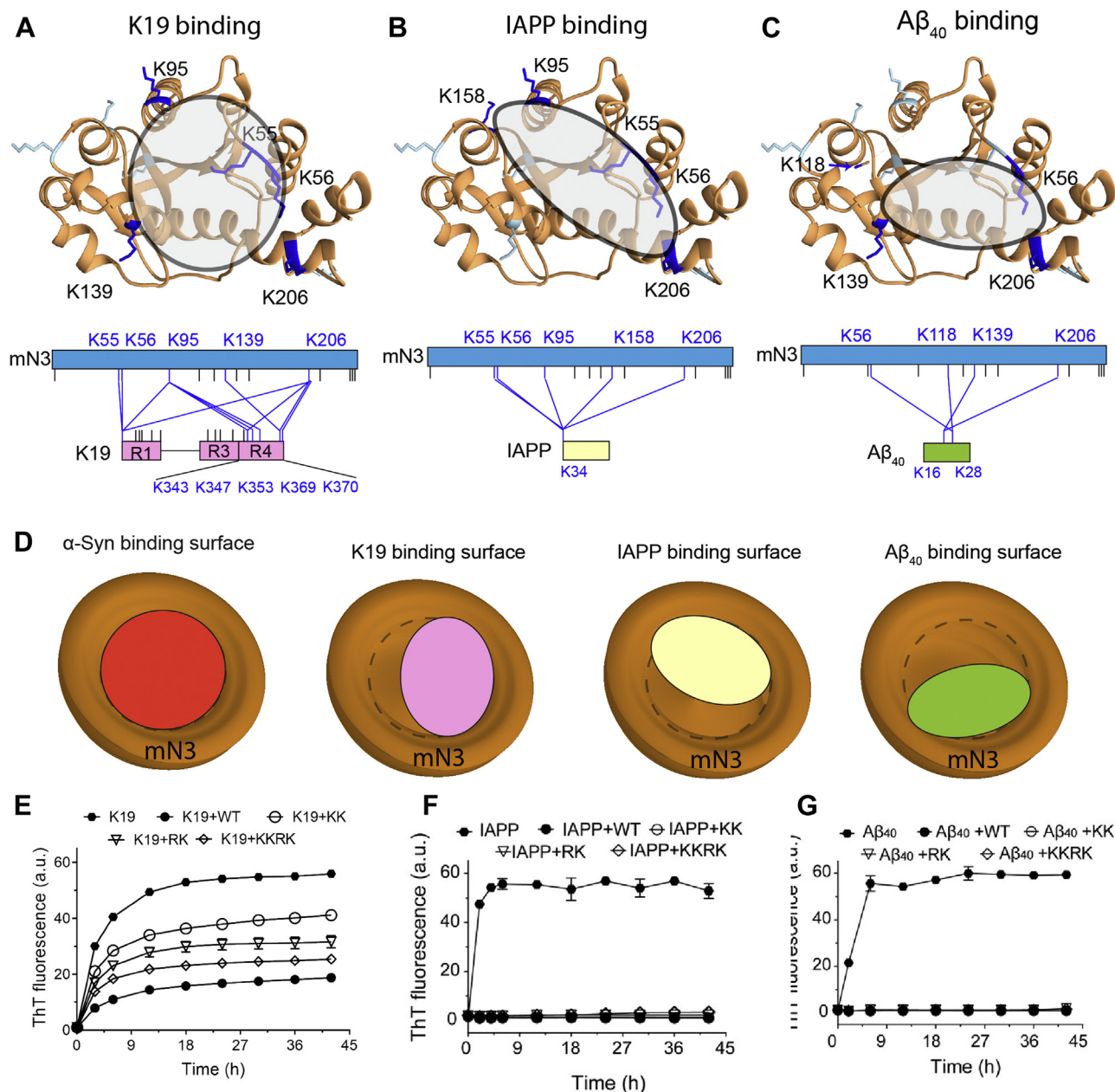 crystal structure of mN3 (PDB ID: 5Z9R) and labeled. Other lysine residues of mN3 are displayed in *light blue*. The enzymatic substrates (ATP/NMN) binding pocket is shaded in *gray*. *B*, the representative structural model of mN3-α-syn$_{111-140}$ complex. The electrostatic surface representation is shown on the *top*. mN3 is shown in hydrophobic surface representation and α-syn$_{111-140}$ is shown in *sticks* (*green*) at the *bottom*. A zoomed-in view of the box region is shown on the *right* with Y136 of α-syn labeled. *C*, influence of NaCl on the inhibition of mN3 to α-syn (100 µM) aggregation (α-syn: mN3 = 5:1). Error bars correspond to mean ± SEM, with n = 3. *D*, effects of mN3 WT and variants to the amyloid aggregation of α-syn (100 µM). The molar ratios of α-syn to mN3 WT and its variants were 5:1, respectively. Error bars correspond to mean ± SD, with n = 3. * indicates $p < 0.05$, ** indicates $p < 0.01$, ns indicates not significant, ## indicates $p < 0.01$ by Brown-Forsythe and Welch *ANOVA* test. *, **, and ns indicates the comparison between WT and mutations, while # indicates the comparison between WT and α-syn only. α-syn, α-synuclein; NMN, nicotinamide mononucleotide.

respectively. CX-MS identified 11 pairs of cross-linked segments between K19 and mN3 with a confidence score of $<10^{-8}$ (Table S2 and Fig. S10). These pairs of segments were cross-linked through five lysine residues (K55, K56, K95, K139, and K206) on mN3 (Fig. 5*A*). Strikingly, this binding surface also localizes at the entrance of the active site of mN3, but a little smaller than that for α-syn binding (Fig. 4*A*). Of note, besides the initial methionine at the N-terminus, five lysine

residues including K343, K347, K353, K369, and K370 within the amyloidogenic R4 region of K19 were identified to cross-linked with mN3 (Fig. 5*A*). These results suggest that mN3 uses its active site to bind the R4 region of K19.

Five pairs of cross-linked segments between IAPP and mN3 were identified using CX-MS with a confidence score of $<10^{-8}$ (Table S2 and Fig. S11). These pairs of segments were cross-linked through five lysine residues including K55, K56, K95,

Figure 5. Client-binding sites of mN3 with three other amyloid client proteins. *A–C*, lysine resides that cross-linked with K19 (*A*), IAPP (*B*), and Aβ40 (*C*) are shown as *sticks* in *blue* in the crystal structure of mN3 (PDB ID: 5Z9R) and labeled. Other lysine residues of mN3 are displayed in *light blue*. The binding surface of mN3 with amyloid client proteins are shaded in *gray*. Schematic profiles of the cross-linked results are shown at the *bottom*. All lysine residues are indicated by *sticks*. The identified cross-linked segments are indicated by *blue lines* and the corresponding linked residues are highlighted in *blue* and labeled. *D*, schematics of mN3 using its active site to bind different amyloid client proteins. The active site is highlighted by the *black dash circle*, while the binding surfaces for α-syn, K19, IAPP, and Aβ40 are shown in *red*, *pink*, *light yellow*, and *light green*, respectively. *e-g*, influences of mN3 WT and variants to the amyloid aggregation of K19 (*E*), IAPP (*F*), and Aβ40 (*G*) measured by ThT fluorescence assays. The molar ratios of K19, IAPP, and Aβ40 to mN3 were 20:1, respectively. Error bars correspond to mean ± SEM, with n = 3. α-syn, α-synuclein; Aβ, amyloid β; IAPP, islet amyloid polypeptide; ThT, thioflavin T.

K158, and K206 of mN3 (Fig. 5*B*). IAPP used in this study is a 37-residue peptide (residues 34–70) with only one lysine (K34) at the N-terminus, thus all the cross-linked segments are though K34 of IAPP (Fig. 5*B*).

Four pairs of cross-linked segments between Aβ40 and mN3 using CX-MS with a confidence score of $<10^{-5}$ were identified (Table S2 and Fig. S12). These pairs of segments were cross-linked through four lysine residues (K56, K118, K139, and K206) of mN3 and two lysine residues (K16 and K28) of Aβ40

(Fig. 5*C*). Strikingly, all of these cross-linked lysine residues with different amyloid client proteins are localized around the active site of mN3 (Figs. 3*A* and 5, *A*–*C*). These results suggest that mN3 uses the similar interface to bind different amyloid client proteins. Intriguingly, the binding interface of mN3 for α-syn is the largest among these four different amyloid client proteins (Fig. 5*D*), which involves six lysine residues and stretches across the entire active site surface of mN3 (Fig. 4*A*). Whereas, mN3 binds K19 and IAPP by using part of this

interface comprising five lysine residues on one side of the active site (Fig. 5, *A* and *B*, *D*), respectively. The interface of mN3 for binding $A\beta_{40}$ is the smallest, which only contains three lysine residues around the active site (Fig. 5, *C* and *D*). Together, the results suggest that mN3 uses different part of the active site as the interface for binding different amyloid client proteins.

We further explored how mutations of the positive-charged residues around the active site influence amyloid aggregation of different client proteins by using the RK, KK, and KKRK mutations. Notably, all these three mN3 mutations exhibit significantly impaired capability in inhibiting K19 aggregation (Fig. 5*E*), indicating the importance of the electrostatic interactions in mN3-K19 binding. In contrast, these mutations do not weaken the inhibitory of mN3 in preventing amyloid aggregation of $A\beta_{40}$ and IAPP (Fig. 5, *F* and *G*), suggesting that these positive-charged residues around the active site is dispensable for mN3 to chaperone $A\beta_{40}$ and IAPP from amyloid aggregation. Thus, mN3 binds different amyloid client proteins by engaging different portions of the active site *via* different types of interactions including electrostatic and hydrophobic interactions for inhibiting amyloid aggregation of different amyloid client proteins.

Discussion

NMNAT has drawn increasing interests since it presents a protective role in various models of neurodegenerative diseases (19–23, 33). Our previous work has demonstrated that NMNAT serves as a chaperone for pTau and uses its active site to specifically bind the phosphorylation sites of pTau to prevent its abnormal aggregation (25). Here, we expand the role of NMNAT as a broad-spectrum chaperone of various pathological amyloid client proteins. We found that mN3 can efficiently inhibit amyloid aggregation of different client proteins including α-syn of PD, $A\beta_{40}$ and Tau (K19) of AD, and IAPP of type II diabetes *in vitro*. Thus, the protective role of NMNAT in various models of neurodegenerative disease may not only from its enzymatic activity of NAD synthesis but also from its chaperone activity in protecting different amyloid client proteins from abnormal aggregation. Interestingly, NMNAT was previously reported to be a cochaperone of Hsp90 to assist the selection of pTau for further clearance (25), indicating the role of NMNAT as a chaperone is more complicated that just simply protecting amyloid client proteins from fibrillation. Mammalian NMNAT exists in three isoforms including N1, N2, and N3, which are found in the nucleus, Golgi apparatus and neuronal axons, and mitochondria, respectively (34). The amyloid client protein α-syn is predominantly localized in the presynaptic termini (35, 36). Interestingly, several studies revealed that α-syn is also localized in neuronal mitochondria in different regions of brains of PD patient and rat (37, 38). α-Syn can also translocate to mitochondria in HEK-293T cells under overexpression conditions (39). Mounting evidence showed that mitochondria dysfunction and α-syn accumulation are closely related in PD pathogenesis (37, 40, 41). Thus, mN3 which is predominantly

localized in mitochondria may chaperone α-syn from aggregation in mitochondria, especially under disease conditions. A fraction of Tau and Aβ are also found in mitochondrial (42–44), implying that mN3 might also play a role in chaperoning them from aggregation. Thus, further cellular and animal studies are needed to investigate the different roles of NMNAT in recognizing and chaperoning different amyloid clients in cells.

Our mechanistic study demonstrates that mN3 uses its active site to bind different amyloid client proteins. Interestingly, mN3 uses different regions of its active site and different types of interactions to mediate its binding with different amyloid client proteins (Fig. 5*C*). Electrostatic interaction is important for the binding between mN3 and clients including α-syn and K19. While, for the amyloid client protein IAPP which contains no negatively charged residue, positively charged residues around the active site of mN3 is not essential in the client binding. Although $A\beta_{40}$ is composed of six negatively charged residues which are evenly distributed on the protein sequence, electrostatic interaction may not be required for the binding of mN3 with $A\beta_{40}$. Instead, hydrophobic interaction may play an important role in binding to these amyloid client proteins. Altogether, the results demonstrate that mN3 is not only an enzyme that involved in the synthesis of NAD but also a broad-spectrum chaperone protecting various amyloid client proteins from abnormal aggregation. mN3 uses the same active site to fulfill its dual function as both an enzyme and a chaperone. Since the active site that synthesizes NAD+ from NMN and ATP is highly conserved in the NMNAT family (25), the other isoforms of NMNAT may also feature a broad-spectrum chaperone activity against various amyloid clients. The dual functions of NMNAT may enable it to be an attractive target in therapy development of related diseases.

Experimental procedures

Protein expression and purification

The preparation of mN1, mN3, and mN3 variants including KK, RK, and KKRK followed the same protocol described previously (25). Briefly, NMNATs and variants were overexpressed in *E. coli* BL21 (DE3) cells, then the protein components were obtained by high pressure crushing. After the purification of HisTrap HP (5 ml) and HiLoad 16/600 Superdex 200 columns (GE Healthcare), the fractions containing purified protein were pooled, concentrated, flash frozen in liquid nitrogen, and stored at −80 °C in a buffer of 50 mM Hepes–KOH, pH 8.0, 150 mM KCl, 10 mM $MgCl_2$, and 5% glycerol.

Human α-syn was expressed and purified as previously described (45). Briefly, α-syn was purified by a HighTrap HP Q (5 ml) column (GE Healthcare) and followed by a Superdex 75 gel filtration column (GE Healthcare). The expression and purification of α-syn$_{1-100}$ was the same as that of α-syn.

Human Tau (K19) was expressed and purified on the basis of a previously described method (46). Briefly, K19 was purified by a HighTrap HP SP (5 ml) column (GE Healthcare) and

followed by a Superdex 75 gel filtration column (GE Healthcare).

Human IAPP (residues 34–70), a 37-amino-acid pancreatic peptide, was purchased from Chinese Peptide Company (AMYN-006). The sequence is below:

KCNTATCATQRLANFLVHSSNNFGAILSSTNVGSNTY-NH$_2$ (C2&C7 Bridge). IAPP was dissolved in hexafluoroisopropanol overnight and then lyophilized.

Human Aβ$_{40}$ was expressed in *E. coli* BL21 Star (DE3) pLysS and purified based on a method described previously (47). Briefly, cells were lysed by a high-pressure homogenizer and centrifuged at 16,000 *rpm* for 30 min. The pellet was washed by 1 M NaCl and Triton X-100 (10% v/v). Then, the pellet was resuspended in 8 M urea, 20 mM Tris–HCl, pH 8.0, and loaded onto a HisTrap HP (5 ml) column (GE Healthcare), then eluted with a pH gradient from 6.0 to 2.0 of 8 M urea, 20 mM Tris–HCl. Eluted proteins were further purified by HPLC (Agilent) and lyophilized.

Hsp27 was expressed and purified using the previously described method (48). Briefly, Hsp27 was purified by a HisTrapFF column (GE Healthcare) and followed by a Superdex 75 gel filtration column (GE Healthcare).

For ^{15}N-labeled proteins, protein expression was the same as that for unlabeled proteins except that the cells were grown in M9 minimal medium with ^{15}NH$_4$Cl (1 g l^{-1}).

The purity of proteins was assessed by SDS-PAGE. Protein concentration was determined by bicinchoninic acid assay (Thermo Fisher).

ThT fluorescence assay

The kinetics of α-syn, K19, Aβ$_{40}$, IAPP, and α-syn$_{1-100}$ fibril formation were monitored using ThT fluorescence assay. The mixture of amyloid client proteins and mN3 WT and variants were added into sealed 384-microwell plates (Greiner Bio-One), which were mixed at the indicated molar ratios in a buffer of 50 mM Tris–HCl, 150 mM NaCl, 0.05% NaN$_3$, pH 8.0. Then, the fluorescence was recorded by a Varioskan Flash Spectral Scanning Multimode Reader (Thermo Fisher Scientific) with shaking at 600 rpm at 37 °C using excitation at 440 nm and emission at 485 nm. To accelerate the fibrillation, 0.5% (v/v) of fibril seeds (the seeds were obtained by sonicating fibrils for 15 s) were added to K19, α-syn, and α-syn$_{1-100}$, respectively. The final concentration of ThT in each sample was 50 μM and three replicates were performed. The ThT results showing the influence of NaCl on the aggregation of α-syn was normalized by the strategy that at each salt concentration, the ThT fluorescence of α-syn with/without mN3 was normalized by using the average ThT value at the end time point (80 h) of the samples without mN3 as 100%.

Transmission electron microscopy

5 μl solution which was obtained at the end time point of the ThT sample was added to fresh glow-discharged 300-mesh copper carbon grids. After being washed with pure water, the copper grids were stained with 3% (v/v) uranyl acetate for 45 s. Specimens were observed using Tecnai G2 Spirit TEM system at 120 kV acceleration voltage. A 4 K × 4K charge-coupled device camera (BM-Eagle, FEI Tecnai) was used to record the images of samples at different magnifications.

Bio-layer interferometry

The binding kinetics of the α-syn to mN3 were measured by BLI on an ForteBio Octet RED96 system (Pall ForteBio LLC). Assays were performed at 37 degree in a 96-well black flat bottom plate (Greiner Bio-One) with orbital shaking at 1000 rpm in an assay buffer of 50 mM Hepes–KOH, 150 mM KCl, 10 mM MgCl$_2$, pH 8.0. α-Syn was firstly biotinylated by incubating 0.5 to 1 mg/ml proteins with biotin at a molar ratio of protein:biotin of 2:3 at 4 °C for 30 min, and then the excess biotins were removed by desalting column (Zeba Spin Desalting Columns, Thermo). Then, biotinylated α-syn proteins were immobilized onto streptavidin biosensors (ForteBio) and incubated with varying concentrations of mN3 as indicated in the figure. The resulting curves were corrected by subtracting the blank reference, then fitted to global fit algorithm using a 1:1 binding assumption to determine the K_D (K_{off}/K_{on}) by the ForteBio Data Analysis software 9.0. The influence of NaCl/ATP/NMN on the binding of α-syn to mN3 was performed by immobilizing biotinylated α-syn onto streptavidin biosensors, then incubated with 2 M folds of mN3 in the absence and presence of NaCl, ATP, and NMN as indicated in the figures, respectively.

NMR spectroscopy

All NMR experiments were performed on a Bruker 900 M or Agilent 800 MHz spectrometer equipped with cryogenic TXI probes at 298 K with the NMR buffer of 25 mM Hepes, 40 mM KCl, 10 mM MgCl$_2$, and 10% (v/v) D$_2$O at pH 7.0. 3D HNCACB and CBCA(CO)NH experiments were performed on ^{15}N^{13}C uniformly labeled α-syn to obtain the chemical shift assignment of backbone atoms of α-syn. The two 3D experiments for α-syn assignment were collected on an Agilent 800 MHz spectrometer equipped with a cryogenic probe. More than 97% of the chemical shift assignments for backbone atoms of α-syn were determined (137/140), with the exception of residues M1, D2, and V3. The backbone assignment of α-syn was consistent with the assignment from the previous study (49). The 2D NMR titration experiments were collected on a Bruker 900 MHz spectrometer or an Agilent 800 MHz spectrometer equipped with a cryogenic probe. Each sample (500 μl) was made of 138 μM ^{15}N-α-syn in the presence of mN3 at 0, 79, 138, and 276 μM, respectively. The influence of NaCl, ATP, and NMN to the interaction between α-syn and mN3 determined by NMR was performed by collecting the HSQC spectra of 50 μM ^{15}N-α-syn alone, and 50 μM ^{15}N-α-syn incubated with 100 μM mN3 in the absence and presence of 100 mM NaCl, 500 μM ATP, and 500 μM NMN, respectively. The CSDs were calculated using the equation,

$$\Delta CSD = \sqrt{(\Delta HN)^2 + (\Delta N/6.5)^2}$$

where ΔHN and ΔN are the CSDs of amide proton and amide nitrogen between free and bound state of α-syn, respectively.

All NMR spectra were processed using NMRPipe (50) and analyzed using Sparky (51) and NMRView (52).

Cross-linking mass spectrometry

Cross-linking experiments were performed as described previously (53). mN3 and amyloid client proteins including α-syn, K19, Aβ$_{40}$, and IAPP were mixed at molar ratios of 1:2, 1:6, 1:5, and 1:8 in a buffer of 50 mM Hepes–KOH (pH 8.0), 150 mM KCl, respectively. Mixtures were incubated for 20 min at 4 °C firstly. Then, 800 μM Cross-linker BS3 (Thermo Fisher Scientific, 21585) was added. The resulting mixtures were incubated at room temperature for 1 h. Twenty millimolar ammonium bicarbonate was added to each sample to quench the cross-linking reaction. The cross-linked samples were pretreated before MS analysis. The proteins were precipitated using acetone, then the pellets were resuspended in a buffer of 100 mM Tris, pH 8.5, 8 M Urea. Hundred millimolar Tris (pH 8.5) was added to make the final concentration of urea to 2 M. TCEP and IAA with final concentrations of 5 mM and 10 mM were added, respectively. Trypsin was added and incubated at 37 °C overnight (16 h) to digest cross-linked proteins. The digested peptides were desalted by a C18 column and then dried by spinning before MS analysis.

The peptides were analyzed by online nanoflow LC–MS/MS. Briefly, nano LC–MS/MS experiments were performed on an EASY-nLC 1000 system (Thermo Scientific) connected to an Orbitrap Q Exactive HF (Thermo Scientific) through a nanoelectrospray ion source. The peptides were separated on a nano column (100 μm × 15 cm, C18, 1.9 μm, 120 Å) and further analyzed using an Orbitrap Q Exactive HF mass spectrometer. One full-scan mass spectrum (350–1500 m/z) at a resolution of 60,000 followed by HCD fragmentation and detection of the fragment ions (scan range from 200 to 2000 m/z) in orbitrap at a 27% normalized collision energy was repeated continuously.

The resulting data were analyzed by pLink (54). The following pLink parameters were used: precursor mass tolerance, 20 ppm; fragment mass tolerance, 10 ppm; cross-linker BS3 (cross-linking sites K and protein N-terminus; xlink mass shift, 138.0680796; monolink mass shift, 156.0786442); fixed modification C, 57.02146; peptide length minimum, four aminoacids per chain; peptide length maximum, 100 aminoacids per chain; peptide mass minimum, 400 Da per chain; and peptide mass maximum, Tsearch (*i.e.*, treat the peptides as protein digestion products using a nonspecific protease). The search results were filtered with a false discovery rate of less than 5% and E values of less than 10^{-5} or 10^{-8}.

Computational modeling of α-syn peptide to mN3

The peptide of C-terminal residues (G111-V140) of α-syn that reveal the biggest CSDs and signal intensity reductions by NMR studies was used to model the complex structure of mN3 and α-syn. The structure coordinates of the C-terminal residues (G111-V140) of α-syn and mN3 were extracted from the structures of α-syn (PDB ID:1XQ8) and mN3 (PDB ID: 5Z9R), respectively. The complex was docked following the same method previously (25) using Rosetta flexile peptide docking (FlexPepDock) protocol (55) in Rosetta software package (31). Five thousand models were generated by using FlexPepDock protocol to simultaneously fold and dock the peptide over the receptor surface. The top models with favorable Rosetta energies and satisfied constrains were selected and further refined by energy minimization. One of the top models ranked by Rosetta energies and constraints was selected for visually inspection.

Data availability

All study data are included in the main text and SI Appendix. The mass spectroscopy raw data have been deposited to the ProteomeXchange with an accession number of PXD031653 (https://www.iprox.cn/page/project.html?id=IPX0004089000).

Author contributions—X. M. and D. L. methodology; C. H., J. L., X. M., and J. Q. investigation; X. M., D. L., and S. Z. writing–original draft; C. H., J. L., X. M., J. Q., C. W., C. L., Y. F., Y. Z., L. J., D. L., and S. Z. formal analysis; C. H., J. L., X. M., J. Q., C. W., C. L., Y. F., Y. Z., L. J., D. L., and S. Z. writing–review and editing.

Conflict of interest—The authors declare that they have no conflict of interests with the contents of this article.

Abbreviations—The abbreviations used are: AD, Alzheimer's disease; Aβ, amyloid β; BLI, bio-layer interferometry; CSD, chemical shift difference; CX-MS, cross-linking mass spectrometry; IAPP, islet amyloid polypeptide; MS, mass spectrometry; NMN, nicotinamide mononucleotide; NMNAT, nicotinamide mononucleotide adenylyltransferase; PD, Parkinson's disease; pTau, phosphorylated Tau; ThT, thioflavin T; α-syn, α-synuclein.

References

1. Hartl, F. U., and Hayer-Hartl, M. (2002) Molecular chaperones in the cytosol: From nascent chain to folded protein. *Science* **295**, 1852
2. Hartl, F. U., Bracher, A., and Hayer-Hartl, M. (2011) Molecular chaperones in protein folding and proteostasis. *Nature* **475**, 324–332

3. Kim, Y. E., Hipp, M. S., Bracher, A., Hayer-Hartl, M., and Ulrich Hartl, F. (2013) Molecular chaperone functions in protein folding and proteostasis. *Annu. Rev. Biochem.* **82**, 323–355

4. Tyedmers, J., Mogk, A., and Bukau, B. (2010) Cellular strategies for controlling protein aggregation. *Nat. Rev. Mol. Cell Biol.* **11**, 777–788

5. Labbadia, J., and Morimoto, R. I. (2015) The biology of proteostasis in aging and disease. *Annu. Rev. Biochem.* **84**, 435–464

6. Muchowski, P. J., and Wacker, J. L. (2005) Modulation of neuro-degeneration by molecular chaperones. *Nat. Rev. Neurosci.* **6**, 11–22

7. Chiti, F., and Dobson, C. M. (2006) Protein misfolding, functional amy-loid, and human disease. *Annu. Rev. Biochem.* **75**, 333–366

8. Sánchez, I., Mahlke, C., and Yuan, J. (2003) Pivotal role of oligomerization in expanded polyglutamine neurodegenerative disorders. *Nature* **421**, 373

9. Selkoe, D. J. (2004) Cell biology of protein misfolding: The examples of Alzheimer's and Parkinson's diseases. *Nat. Cell Biol.* **6**, 1054–1061

10. Jackrel, M. E., and Shorter, J. (2017) Protein-remodeling factors as po-tential therapeutics for neurodegenerative disease. *Front. Neurosci.* **11**, 99

11. Auluck, P. K., Chan, H. Y., Trojanowski, J. Q., Lee, V. M., and Bonini, N. M. (2002) Chaperone suppression of alpha-synuclein toxicity in a Drosophila model for Parkinson's disease. *Science* **295**, 865–868

12. Dickey, C. A., Kamal, A., Lundgren, K., Klosak, N., Bailey, R. M., Dun-more, J., Ash, P., Shoraka, S., Zlatkovic, J., Eckman, C. B., Patterson, C., Dickson, D. W., Nahman, N. S., Jr., Hutton, M., Burrows, F., *et al.* (2007) The high-affinity HSP90-CHIP complex recognizes and selectively de-grades phosphorylated tau client proteins. *J. Clin. Invest.* **117**, 648–658

13. Mok, S. A., Condello, C., Freilich, R., Gillies, A., Arhar, T., Oroz, J., Kadavath, H., Julien, O., Assimon, V. A., Rauch, J. N., Dunyak, B. M., Lee, J., Tsai, F. T. F., Wilson, M. R., Zweckstetter, M., *et al.* (2018) Mapping interactions with the chaperone network reveals factors that protect against tau aggregation. *Nat. Struct. Mol. Biol.* **25**, 384–393

14. Wentink, A. S., Nillegoda, N. B., Feufel, J., Ubartaite, G., Schneider, C. P., De Los Rios, P., Hennig, J., Barducci, A., and Bukau, B. (2020) Molecular dissection of amyloid disaggregation by human HSP70. *Nature* **587**, 483–488

15. Jia, C., Ma, X., Liu, Z., Gu, J., Zhang, X., Li, D., and Zhang, S. (2019) Different heat shock proteins bind alpha-synuclein with distinct mecha-nisms and synergistically prevent its amyloid aggregation. *Front. Neurosci.* **13**, 1124

16. Lackie, R. E., Maciejewski, A., Ostapchenko, V. G., Marques-Lopes, J., Choy, W. Y., Duennwald, M. L., Prado, V. F., and Prado, M. A. M. (2017) The Hsp70/Hsp90 chaperone machinery in neurodegenerative diseases. *Front. Neurosci.* **11**, 254

17. Diane, A., Abunada, H., Khattab, N., Moin, A. S. M., Butler, A. E., and Dehbi, M. (2021) Role of the DNAJ/HSP40 family in the pathogenesis of insulin resistance and type 2 diabetes. *Ageing Res. Rev.* **67**, 101313

18. Magni, G., Amici, A., Emanuelli, M., Raffaelli, N., and Ruggieri, S. (1999) Enzymology of NAD+ synthesis. *Adv. Enzymol. Relat. Areas Mol. Biol.* **73**, 135

19. Zhai, R. G., Zhang, F., Hiesinger, P. R., Cao, Y., Haueter, C. M., and Bellen, H. J. (2008) NAD synthase NMNAT acts as a chaperone to protect against neurodegeneration. *Nature* **452**, 887

20. Ali, Y. O., Ruan, K., and Zhai, R. G. (2012) NMNAT suppresses Tau-induced neurodegeneration by promoting clearance of hyper-phosphorylated Tau oligomers in a Drosophila model of tauopathy. *Hum. Mol. Genet.* **21**, 237–250

21. Ljungberg, M. C., Ali, Y. O., Zhu, J., Wu, C.-S., Oka, K., Zhai, R. G., and Lu, H.-C. (2012) CREB-activity and nmnat2 transcription are down-regulated prior to neurodegeneration, while NMNAT2 over-expression is neuroprotective, in a mouse model of human tauopathy. *Hum. Mol. Genet.* **21**, 251–267

22. Ali, Y. O., Allen, H. M., Yu, L., Li-Kroeger, D., Bakhshizadehmahmoudi, D., Hatcher, A., McCabe, C., Xu, J., Bjorklund, N., Taglialatela, G., Ben-nett, D. A., De Jager, P. L., Shulman, J. M., Bellen, H. J., and Lu, H.-C. (2016) NMNAT2:HSP90 complex mediates proteostasis in proteino-pathies. *PLoS Biol.* **14**, e1002472

23. Rossi, F., Geiszler, P. C., Meng, W., Barron, M. R., Prior, M., Herd-Smith, A., Loreto, A., Lopez, M. Y., Faas, H., Pardon, M.-C., and Conforti, L. (2018) NAD-biosynthetic enzyme NMNAT1 reduces early behavioral impairment in the htau mouse model of tauopathy. *Behav. Brain Res.* **339**, 140–152

24. Ali, Y. O., Li-Kroeger, D., Bellen, H. J., Zhai, R. G., and Lu, H.-C. (2013) NMNATs, evolutionarily conserved neuronal maintenance factors. *Trends Neurosci.* **36**, 632–640

25. Ma, X., Zhu, Y., Lu, J., Xie, J., Li, C., Shin, W. S., Qiang, J., Liu, J., Dou, S., Xiao, Y., Wang, C., Jia, C., Long, H., Yang, J., Fang, Y., *et al.* (2020) Nicotinamide mononucleotide adenylyltransferase uses its NAD(+) substrate-binding site to chaperone phosphorylated Tau. *Elife* **9**, e51859

26. Spillantini, M. G., Schmidt, M. L., Lee, V. M. Y., Trojanowski, J. Q., Jakes, R., and Goedert, M. (1997) α-Synuclein in Lewy bodies. *Nature* **388**, 839

27. Bloom, G. S. (2014) Amyloid-beta and tau: The trigger and bullet in Alzheimer disease pathogenesis. *JAMA Neurol.* **71**, 505–508

28. Marzban, L., Park, K., and Verchere, C. B. (2003) Islet amyloid poly-peptide and type 2 diabetes. *Exp. Gerontol.* **38**, 347–351

29. Spillantini, M. G., and Goedert, M. (2000) The alpha-synucleinopathies: Parkinson's disease, dementia with Lewy bodies, and multiple system atrophy. *Ann. N. Y Acad. Sci.* **920**, 16–27

30. Ehrnhoefer, D. E., Bieschke, J., Boeddrich, A., Herbst, M., Masino, L., Lurz, R., Engemann, S., Pastore, A., and Wanker, E. E. (2008) EGCG redirects amyloidogenic polypeptides into unstructured, off-pathway oligomers. *Nat. Struct. Mol. Biol.* **15**, 558–566

31. Leaver-Fay, A., Tyka, M., Lewis, S. M., Lange, O. F., Thompson, J., Jacak, R., Kaufman, K., Renfrew, P. D., Smith, C. A., Sheffler, W., Davis, I. W., Cooper, S., Treuille, A., Mandell, D. J., Richter, F., *et al.* (2011) ROSETTA3: An object-oriented software suite for the simulation and design of macromolecules. *Methods Enzymol.* **487**, 545–574

32. Zhang, X., Kurnasov, O. V., Karthikeyan, S., Grishin, N. V., Osterman, A. L., and Zhang, H. (2003) Structural characterization of a human cytosolic NMN/NaMN adenylyltransferase and implication in human NAD biosynthesis. *J. Biol. Chem.* **278**, 13503–13511

33. Brazill, J. M., Li, C., Zhu, Y., and Zhai, R. G. (2017) NMNAT: It's an NAD+ synthase… It's a chaperone… It's a neuroprotector. *Curr. Opin. Genet. Dev.* **44**, 156–162

34. Berger, F., Lau, C., Dahlmann, M., and Ziegler, M. (2005) Subcellular compartmentation and differential catalytic properties of the three hu-man nicotinamide mononucleotide adenylyltransferase isoforms. *J. Biol. Chem.* **280**, 36334–36341

35. Murphy, D. D., Rueter, S. M., Trojanowski, J. Q., and Lee, V. M. (2000) Synucleins are developmentally expressed, and alpha-synuclein regulates the size of the presynaptic vesicular pool in primary hippocampal neu-rons. *J. Neurosci.* **20**, 3214–3220

36. Iwai, A., Masliah, E., Yoshimoto, M., Ge, N., Flanagan, L., de Silva, H. A., Kittel, A., and Saitoh, T. (1995) The precursor protein of non-A beta component of Alzheimer's disease amyloid is a presynaptic protein of the central nervous system. *Neuron* **14**, 467–475

37. Devi, L., Raghavendran, V., Prabhu, B. M., Avadhani, N. G., and Anandatheerthavarada, H. K. (2008) Mitochondrial import and accu-mulation of alpha-synuclein impair complex I in human dopaminergic neuronal cultures and Parkinson disease brain. *J. Biol. Chem.* **283**, 9089–9100

38. Zhang, L., Zhang, C., Zhu, Y., Cai, Q., Chan, P., Ueda, K., Yu, S., and Yang, H. (2008) Semi-quantitative analysis of alpha-synuclein in subcellular pools of rat brain neurons: An immunogold electron microscopic study using a C-terminal specific monoclonal antibody. *Brain Res.* **1244**, 40–52

39. Shavali, S., Brown-Borg, H. M., Ebadi, M., and Porter, J. (2008) Mito-chondrial localization of alpha-synuclein protein in alpha-synuclein overexpressing cells. *Neurosci. Lett.* **439**, 125–128

40. Camilleri, A., and Vassallo, N. (2014) The centrality of mitochondria in the pathogenesis and treatment of Parkinson's disease. *CNS Neurosci. Ther.* **20**, 591–602

41. Park, J. H., Burgess, J. D., Faroqi, A. H., DeMeo, N. N., Fiesel, F. C., Springer, W., Delenclos, M., and McLean, P. J. (2020) Alpha-synuclein-induced mitochondrial dysfunction is mediated *via* a sirtuin 3-dependent pathway. *Mol. Neurodegener.* **15**, 5

42. Cieri, D., Vicario, M., Vallese, F., D'Orsi, B., Berto, P., Grinzato, A., Catoni, C., De Stefani, D., Rizzuto, R., Brini, M., and Cali, T. (2018) Tau localises within mitochondrial sub-compartments and its caspase cleav-age affects ER-mitochondria interactions and cellular Ca(2+) handling. *Biochim. Biophys. Acta Mol. Basis Dis.* **1864**, 3247–3256

43. Manczak, M., Anekonda, T. S., Henson, E., Park, B. S., Quinn, J., and Reddy, P. H. (2006) Mitochondria are a direct site of A beta accumulation in Alzheimer's disease neurons: Implications for free radical generation and oxidative damage in disease progression. *Hum. Mol. Genet.* **15**, 1437–1449

44. Caspersen, C., Wang, N., Yao, J., Sosunov, A., Chen, X., Lustbader, J. W., Xu, H. W., Stern, D., McKhann, G., and Yan, S. D. (2005) Mitochondrial Abeta: A potential focal point for neuronal metabolic dysfunction in Alzheimer's disease. *FASEB J.* **19**, 2040–2041

45. Jakes, R., Spillantini, M. G., and Goedert, M. (1994) Identification of two distinct synucleins from human brain. *FEBS Lett.* **345**, 27–32

46. Barghorn, S., Biernat, J., and Mandelkow, E. (2005) Purification of recombinant tau protein and preparation of Alzheimer-paired helical filaments *in vitro*. *Methods Mol. Biol. (Clifton, N.J.)* **299**, 35–51

47. Walsh, D. M., Thulin, E., Minogue, A. M., Gustavsson, N., Pang, E., Teplow, D. B., and Linse, S. (2009) A facile method for expression and purification of the Alzheimer's disease-associated amyloid beta-peptide. *FEBS J.* **276**, 1266–1281

48. Liu, Z., Zhang, S., Gu, J., Tong, Y., Li, Y., Gui, X., Long, H., Wang, C., Zhao, C., Lu, J., He, L., Li, Y., Liu, Z., Li, D., and Liu, C. (2020) Hsp27 chaperones FUS phase separation under the modulation of stress-induced phosphorylation. *Nat. Struct. Mol. Biol.* **27**, 363–372

49. Rao, J. N., Kim, Y. E., Park, L. S., and Ulmer, T. S. (2009) Effect of pseudorepeat rearrangement on alpha-synuclein misfolding, vesicle binding, and micelle binding. *J. Mol. Biol.* **390**, 516–529

50. Delaglio, F., Grzesiek, S., Vuister, G. W., Zhu, G., Pfeifer, J., and Bax, A. (1995) NMRPipe: A multidimensional spectral processing system based on UNIX pipes. *J. Biomol. NMR* **6**, 277

51. Lee, W., Tonelli, M., and Markley, J. L. (2015) NMRFAM-SPARKY: Enhanced software for biomolecular NMR spectroscopy. *Bioinformatics* **31**, 1325

52. Johnson, B. A. (2004) Using NMRView to visualize and analyze the NMR spectra of macromolecules. *Methods Mol. Biol.* **278**, 313

53. Zhou, G., Ding, Y. H., Xu, D., Na, L., Zhang, E. E., Dong, M. Q., and Tang, C. (2015) Visualizing the ensemble structures of protein complexes using chemical cross-linking coupled with mass spectrometry. *Biophys. Rep.* **1**, 127–138

54. Yang, B., Wu, Y. J., Zhu, M., Fan, S. B., Lin, J., Zhang, K., Li, S., Chi, H., Li, Y. X., Chen, H. F., Luo, S. K., Ding, Y. H., Wang, L. H., Hao, Z., Xiu, L. Y., *et al*. (2012) Identification of cross-linked peptides from complex samples. *Nat. Methods* **9**, 904–906

55. Raveh, B., London, N., Zimmerman, L., and Schueler-Furman, O. (2011) Rosetta FlexPepDock ab-initio: Simultaneous folding, docking and refinement of peptides onto their receptors. *PLoS one* **6**, e18934